

Modelling of dense particle-laden pipe flow and a free jet

G. Mallouppas* and B.G.M. van Wachem*

* Department of Mechanical Engineering, Imperial College London, London, SW7 2AZ, United Kingdom

george.mallouppas05@imperial.ac.uk and b.van-wachem@imperial.ac.uk

Keywords: Lagrangian simulations, particle-laden gas, LES, Discrete Element Method

Abstract

In this contribution, we have performed Large Eddy Simulations (LES) of the dense particle laden turbulent flow as described by prof. Jennifer Sinclair Curtis (University of Florida, USA) and co-workers. The fluid phase is modelled with three different LES models, *i.e.* a Smagorinsky model where van Driest dampening is employed near the walls, and the more recent WALE and Vreman models. Also, the effect of mesh spacing on the flow prediction is researched. The particles are modelled by the Discrete Element Model (DEM), in which the particle collisions are approximated by their local elastic and plastic deformation. The importance of collisions is shown by comparing the simulations taking particle collisions into account to simulations neglecting this effect. The effect of the geometry is also researched. Due to the dimensions of the box in which the turbulent pipe flow enters, it is expected that this dimension has a significant effect on the spreading rate of the turbulent gas-particle jet. Finally, the particle size is varied, in accordance with the available experimental data. The particles used in the simulations range from 25 μm to 70 μm as well as a mixture of these. All findings are compared with the experimental data.

Nomenclature

Roman symbols

c	Vreman constant (–)
d	diameter (m)
g	gravitational constant (ms^{-1})
p	pressure (Nm^{-2})
m	solids loading (–)
v	velocity (ms^{-1})
u_τ	friction velocity (ms^{-1})
C_D	Drag coefficient (–)
C_{SGS}	Smagorinsky constant (–)
C_{vD}	Smagorinsky van Driest constant (–)
C_w	Wale constant (–)
E	Young's modulus (Nm^{-2})
G	shear modulus (Nm^{-2})
R	pipe radius (m)
Re	Reynolds number (–)
S_f	Source term linear in velocity ($\text{kgm}^{-3}\text{s}^{-1}$)
T	Torque (Nm)
T_f^j	Additional source terms ($\text{kgm}^{-2}\text{s}^{-2}$)

Greek symbols

α	local volume fraction (–)
β	drag function ($\text{kgm}^{-3}\text{s}^{-1}$)
κ	von Karman constant (–)
μ	viscosity (Nsm^{-2})

ν	kinematic viscosity (m^2s^{-1})
τ	Stress tensor of the fluid (Nm^{-2})
ρ	density (kgm^{-3})
σ	Poisson's ratio (–)
ω	angular velocity (rads^{-1})
Δ	filter width (m)

Subscripts

f	Gas
p	Particle

Superscripts

g	Gas
p	Particle

Introduction

Particle-laden turbulent flows can be found in various industrial and environmental processes. Examples of such processes are pneumatic transport, fluidised beds; energy generation of fossil fuels; movement of soot particles in the atmosphere; the flow of particles in cyclones and many more. Understanding particle-particle, particle-fluid and particle-wall interactions is of utmost importance as a more accurate implementation of these processes will result in more reliable analysis

tools of such flows. Reliable numerical simulations will therefore help the optimisation and better design of industrial processes and also reliable prediction of environmental processes.

There are various frameworks in which gas-solid flows can be predicted in the Eulerian-Lagrangian framework, *e.g.* Large Eddy Simulation (LES), Direct Numerical Simulation (DNS) and the Reynolds Averaged Navier-Stokes (RANS) method. RANS methods do not resolve the small scales, which are important for turbulent flows, but only consider the averaged quantities of the transport equations. The smaller scales are modelled by appropriate closure models. DNS methods, on the other hand, offer much higher accuracy in solving the Navier-Stokes equations at the expense of huge computational time; currently, DNS can only solve flows of low Reynolds (Re) numbers, which are outside of most the engineering and industrial interests. Although the computational effort for LES is still very high, it is considerably lower than for DNS and therefore has become very fashionable for analysis of flows in research and is an emerging tool in industrial problems.

LES solves the Navier-Stokes equations up to a particular length-scale due to the application of a filter. Length-scales smaller than the cut-off width (Δ) of the filter are modelled. This cut-off width is an indication of the size of eddies that are retained in the computations and the size of eddies that are rejected Versteeg and Malalasekera (2007). Due to the filtering of the Navier-Stokes equations, models are required to resolve the sub-grid-scale (SGS) stresses to account for the effect of unresolved scales on the convective momentum transport. In this paper, three different models are used and compared with one another. These models are the well known Smagorinsky model where van Driest damping is employed near the wall; the Wall-Adapting Local-Eddy (WALE) viscosity model proposed by Nicoud et al Nicoud and Durcos (1999); and finally the Vreman model proposed by Vreman Vreman (2004).

The particle interactions are modelled by the Discrete Element Model (DEM), first applied by Cundall and Strack Cundall and Strack (1979). The particle-particle and particle-wall collisions are approximated by the elastic and plastic deformation occurring during collision. Such deformation is mathematically described by a spring-dashpot-slider model, or soft-sphere model, as proposed by Tsuji et al. Tsuji et al. (1991).

Due to the large number of particles, the computational time and memory space required for these

simulations is very large. This is because computations for each particle take place for every timestep. On the other hand, DEM has a very high accuracy as no empirical data, besides from material properties, are required to predict the particle-particle and particle-wall interactions. The model is also fully deterministic - making an accurate comparison of the effect of initial conditions possible. To describe the fluid-particle interactions, the Wen and Yu Wen and Yu (1966) drag force has been employed in this work. Although accounting for the volume fraction effects on the drag force is probably not of large importance in the test-cases simulated in the current research work, it might have an effect on the particle-clustering. The forces resulting from the fluid-particle interactions, the particle-particle interactions and the particle-wall interactions are added and used to track the individual particles employing the Verlet integration scheme.

Theory

Fluid-phase modelling

The equations for the fluid-phase are similar to the single-phase, except for including a local volume fraction and including source terms accounting for the presence of particles. The governing equations are the mass continuity and conservation of momentum, which are given by equations (1) & (2) respectively,

$$\frac{\partial(\alpha_f \rho_f)}{\partial t} + \frac{\partial(\alpha_f \rho_f v_f^i)}{\partial x^i} = 0 \quad (1)$$

and

$$\begin{aligned} \frac{\partial(\alpha_f \rho_f v_f^j)}{\partial t} + \frac{\partial(\alpha_f \rho_f v_f^j v_f^i)}{\partial x^i} &= \frac{\partial(\alpha_f \tau_f^{ij})}{\partial x^i} - \alpha_f \frac{\partial p}{\partial x^j} \\ &+ S_f v_f^j + T_f^j + \sum_{p=1}^{phases \neq f} \beta_{(f,p)} [v_f^j - v_p^j] \end{aligned} \quad (2)$$

where α_f is the local volume fraction of the fluid phase; S_f the source term linear in the velocity field; T_f^j the additional source terms; and τ_f^{ij} the stress tensor of the fluid, given by

$$\tau_f^{ij} = \mu_f \left(\frac{\partial v^i}{\partial x^j} + \frac{\partial v^j}{\partial x^i} \right) + \delta_{ij} \left(\lambda_f - \frac{2}{3} \mu_f \right) \frac{\partial v^k}{\partial x^k} \quad (3)$$

where μ_f is the shear and λ_f represent the bulk viscosity of the fluid.

Subgrid Scale Models

Large Eddy Simulation (LES) is used to solve the mass-continuity and momentum equations, models are

therefore needed to determine the subgrid-scale (SGS) stresses. Three models are used and compared with experimental data. These are the Smagorinsky model with van Driest damping near the wall; the WALE model Nicoud and Durcos (1999); and finally the Vreman model Vreman (2004). It is worthwhile mentioning that the models are compared with one another by considering two different geometries, by varying the length of the inlet pipe. Predictions have been made for an inlet pipe of length $\frac{L}{D} = 20.0$ and of $\frac{L}{D} = 90.0$. In addition, different mesh spacing is researched in order to examine the effect on the flow prediction.

Van Driest Wall damping

It is well-known that the Smagorinsky model is not suitable to account for the effect of walls, as the strong velocity gradient perpendicular to the wall is present due to the no-slip boundary condition at the wall and not a gradient driving the turbulence. Hence, near the wall the so-called van Driest dampening is employed which is based upon a simple mixing length model.

Prandtl's mixing-length hypothesis Wilcox (1998); Pope (2000) states that,

$$\tau_{xy} = \mu_T \frac{dU}{dy} \quad (4)$$

where y is the length from the wall, in the case of pipe flow given by,

$$y = (R - r) \quad (5)$$

and μ_T represents the eddy viscosity, which is

$$\mu_T = l_{mix}^2 \left| \frac{dU}{dy} \right| \quad (6)$$

where l_{mix}^2 is the mixing length. The mixing length scale is approximated as

$$l_{mix} = \kappa y \quad (7)$$

Near the wall, however, l_{mix} is not well described by Equation (7). This is because the mixing length model 'seems incapable of reproducing the y^{+3} variation near the wall' Grifoll and Giralt (2000). The mixing length is, therefore, modified by the van Driest damping function. This function dampens the effect of viscosity near the wall. Hence equation (7) is modified to equation (8)

$$l_{mix} = \kappa y \left[1 - e^{-y^+/A_o^+} \right] \quad (8)$$

where y^+ is the dimensionless distance defined as,

$$y^+ = \frac{u_\tau y}{\nu_f} \quad (9)$$

and A_o^+ is a constant, typically $A_o^+ = 26$. Although the model seems very crude, it has proven to be quite successful in many types of wall bounded turbulent flows.

Smagorinsky model

The Smagorinsky model assumes that the local SGS stresses are proportional to the local rate of strain of the resolved flow Versteeg and Malalasekera (2007). Thus, the stresses are given as

$$\tau_{ij}^a = -2\mu_{SGS}\bar{S}_{ij} + \frac{1}{3}\tau_{il}\delta_{ij} \quad (10)$$

where $\bar{S}_{ij} = \frac{1}{2} \left[\frac{\partial \bar{u}_i}{\partial x_j} + \frac{\partial \bar{u}_j}{\partial x_i} \right]$. μ_{SGS} is estimated using equation (11)

$$\mu_{SGS} = \rho_f (C_{SGS} \Delta)^2 \sqrt{2\bar{S}_{ij}\bar{S}_{ij}} \quad (11)$$

where C_{SGS} is the Smagorinsky constant, Δ is the LES filter width.

The Smagorinsky - van Driest constant The Smagorinsky model, however, does not accurately represent the eddy viscosity near the wall. As shown by Weickert et al Weickert et al. (2009), the C_{SGS} is modified as,

$$C_{vD} = C_{SGS} \Delta (1 - e^{-\delta_v^+/A_o^+}) \quad (12)$$

In the simulation the following constants were used; $C_{SGS} = 0.142$ and $A_o^+ = 25.0$. Note that $\delta_v^+ = \frac{u_\tau \delta_v}{\nu_f}$. μ_{SGS} is,

$$\mu_{SGS} = \rho_f C_{vD}^2 \sqrt{2\bar{S}_{ij}\bar{S}_{ij}} \quad (13)$$

WALE model

Nicoud et al Nicoud and Durcos (1999) proposed the wall-adapting local eddy-viscosity (WALE) model. With this model, the non-physical behaviour of the eddy viscosity as predicted by the Smagorinsky model near the wall is avoided. This is because the WALE model is of higher order compared to the Smagorinsky model, which is $O(1)$. In this way, the eddy viscosity at the wall is zero and hence, the only viscosity contribution at the wall is the molecular viscosity. The model for the eddy viscosity is given in Nicoud and Durcos (1999) and Weickert et al. (2009),

$$\mu_{SGS} = \rho_f (C_w \Delta)^2 \frac{(S_{ij}^d S_{ij}^d)^{\frac{3}{2}}}{(\bar{S}_{ij} \bar{S}_{ij})^{\frac{5}{2}} + (S_{ij}^d S_{ij}^d)^{\frac{5}{4}}} \quad (14)$$

C_w is related to the Smagorinsky constant via,

$$C_w^2 = C_{SGS}^2 \frac{\langle \sqrt{2}(\bar{S}_{ij} \bar{S}_{ij})^{\frac{3}{2}} \rangle}{\langle \bar{S}_{ij} \bar{S}_{ij} \frac{(S_{ij}^d S_{ij}^d)^{\frac{3}{2}}}{(\bar{S}_{ij} \bar{S}_{ij})^{\frac{5}{2}} + (S_{ij}^d S_{ij}^d)^{\frac{5}{4}}} \rangle} \quad (15)$$

with $S_{ij}^d = \frac{1}{2}(\bar{g}_{ij}^2 + \bar{g}_{ji}^2) - \frac{1}{3}\delta_{ij}\bar{g}_{kk}^2$ and $\bar{g}_{ij} = \frac{\partial \bar{u}_i}{\partial x_j}$.

Vreman model

Vreman Vreman (2004) proposed an eddy viscosity model used in LES, which is also of higher order accuracy and produces the correct limit of the eddy viscosity near the walls. This model assumes that the dissipation is relatively small in transitional and near-wall regions. The eddy viscosity is calculated as

$$\mu_{SGS} = \rho_f c \sqrt{\frac{B_\beta}{\alpha_{ij}\alpha_{ij}}} \quad (16)$$

with $\alpha_{ij} = \frac{\partial \bar{u}_i}{\partial x_j}$, $\beta_{ij} = \Delta_m^2 \alpha_{mi}\alpha_{mj}$ and $B_\beta = \beta_{11}\beta_{22} - \beta_{12}^2 + \beta_{11}\beta_{33} - \beta_{13}^2 + \beta_{22}\beta_{33} - \beta_{23}^2$. The model constant c is related to the Smagorinsky constant as $c \approx 2.5C_{SGS}^2$.

Filtering Method

LES utilises low-pass filters so that only the large scale eddies are resolved, whereas the smaller scale eddies are removed. In the aforementioned models, a filter width is used in order to define the cut-off lengthscale. In this paper the volume of the cells used in the meshing is directly related to the filter width (Δ), i.e. $\Delta = \sqrt[3]{V_{cell}}$. As for successful LES calculations, the computational cell aspect ratio has to remain near unity, this is a good approximation.

Particle modelling

A discrete element model (DEM) proposed by Cundall and Strack Cundall and Strack (1979) is used to model the particles. The individual trajectories of the particles are determined in the Lagrangian framework, where particle collisions are modelled via the soft-sphere model proposed by Tsuji et al Tsuji et al. (1991), which accounts for some non-reversible deformation.

Discrete Element Models (DEM) The interactions of particles with other particles and walls are of dynamic nature. This is because the particle movements are essentially defined by the particle-particle interactions; particle-wall interactions; particle-fluid interactions and/or body forces Kuang et al. (2008). The trajectories of individual particles are considered (i.e. described in a Lagrangian framework) and Newton's 2nd law is solved for each individual particle, accounting for the fluid-particle, particle-particle, and particle-wall interactions, and approximating the integral with the Verlet algorithm. The flowchart shown in figure 1 illustrates the DEM algorithm. The flowchart describes the logic of how forces between

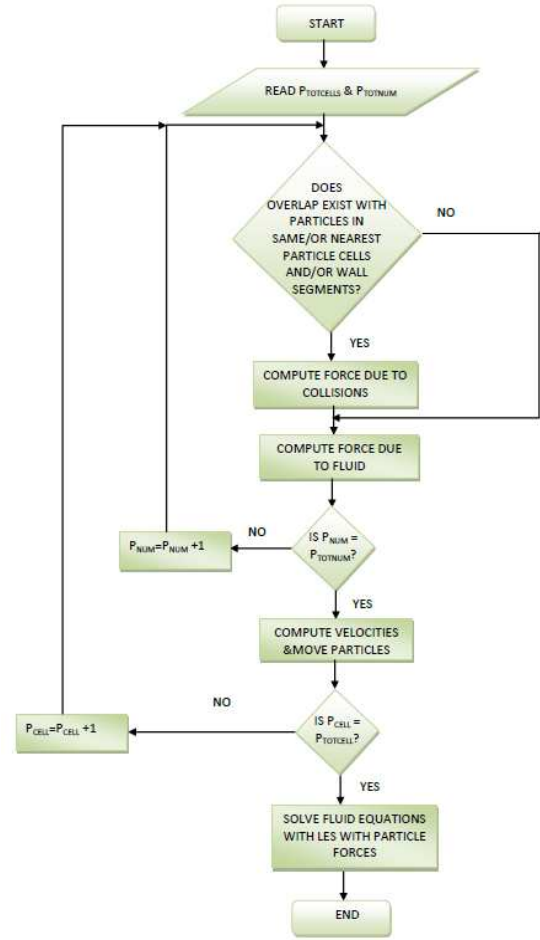


Figure 1: DEM flowchart at a single timestep.

individual particles with other particles and/or walls of the domain are determined. In addition, it illustrates how forces between particles and the fluid are computed.

Newton's 2nd law for the particles is written out as

$$m_p \frac{d\mathbf{v}_p}{dt} = \beta \frac{V_p}{\alpha_p} (\mathbf{v}_f - \mathbf{v}_p) + m_p \mathbf{g} - V_p \nabla P_f + \sum^N [\mathbf{F}_{pw} + \mathbf{F}_{pp}] \quad (17)$$

and for the rotational momentum

$$I_p \frac{d\boldsymbol{\omega}_p}{dt} = \mathbf{T}_p \quad (18)$$

where m_p is the mass of the particle; I_p is the momentum of rotational inertia; \mathbf{T}_p the torque of the particle; $\boldsymbol{\omega}_p$ is rotational velocity; \mathbf{v}_p is the translational velocity; and β is the drag function as proposed by Wen and Yu Wen and Yu (1966), where the reciprocal of the Eulerian

Table 1: Terms of right hand side of equation (17).

Term	Force Type
$\beta \frac{V_p}{\alpha_p} (\mathbf{v}_f - \mathbf{v}_p)$	Drag force
$m_p \mathbf{g}$	Body force due to gravity
$V_p \nabla P_f$	Force due to the pressure gradient
\mathbf{F}_{pw}	Particle-wall contact force
\mathbf{F}_{pp}	Particle-particle contact force

fluid-particle timescale is given by

$$\beta = \frac{3}{4} C_D \frac{\alpha_p \alpha_f \rho_f |\mathbf{v}_f - \mathbf{v}_p|}{d_p} \alpha_f^{-2.65} \quad (19)$$

and C_D represents the coefficient of drag for an individual particle and α_f represents the fluid volume fraction. The right hand side terms of equation (17) are outlined in table 1.

Implementation of particle collisions The particle-particle and particle-wall interactions as taken into account in this work are assumed to be local; *i.e.* no long-range forces are included. For establishing the nature of the interaction, each particle pair could be interrogated. However, this would lead to a scaling of the computational effort with N^2 , N being the number of particles. Instead, a particle-mesh algorithm is adopted, in which each of the particles is assigned a cell in the particle mesh based upon its location. Using this particle-mesh, each particle is only tested for interaction against particles located in the same or directly neighbouring particle mesh cells. Although there is some additional computational effort and a slightly more complex algorithm required for this approach, it leads to a scaling of $N \log N$ with the number of particles, making it a lot more favourable for large numbers of particles.

The particle collisions are modelled by the soft-sphere model as described by Cundall and Strack Cundall and Strack (1979). In brief, this model uses a spring-dashpot-slider arrangement to describe the particle behaviour before, during and after a collision. The damping coefficient used, described by Tsuji et al Tsuji (1994) & Tsuji et al. (1991) is, however, used since it is related to the coefficient of restitution.

The normal and tangential contact forces are given by the sum of forces due to the spring and dashpot. From Hertzian contact theory the normal and tangential contact forces are,

$$\mathbf{F}_{nij} = (-k_n \delta^{\frac{3}{2}} - \eta_{nj} \mathbf{G} \cdot \mathbf{n}) \mathbf{n} \quad (20)$$

$$\mathbf{F}_{tij} = -k_t \delta_t - \eta_{tj} \mathbf{G}_{ct} \quad (21)$$

where \mathbf{G} is the velocity vector of particle i relative to particle j , \mathbf{G}_{ct} is the slit velocity vector at the contact point. The subscripts n and t represent the normal and tangential components respectively and δ is the displacement, or overlap, of particles i and j during collision. Three parameters are required by the soft-sphere model; stiffness (k), damping coefficient (η) and the coefficient of friction (μ). μ is a well known empirical quantity, stiffness and the damping coefficient must be estimated using equations

$$\eta_n = \alpha \sqrt{M k_n} \delta^{\frac{1}{4}} \quad (22)$$

$$\eta_t = \alpha \sqrt{M k_t} \delta^{\frac{1}{4}} \quad (23)$$

where $M = \frac{m_i m_j}{m_i + m_j}$; and m is the mass of the particle. Note that for wall collisions $m_w \rightarrow \infty$, hence $M = m_p$. The relationship between α and the coefficient of restitution is well defined by Tsuji et al Tsuji et al. (1991). The spring constants are, based upon elastic deformation,

$$k_n = \frac{4}{3} \left(\frac{1 - \sigma_i^2}{E_i} + \frac{1 - \sigma_j^2}{E_j} \right)^{-1} \left(\frac{r_i + r_j}{r_i r_j} \right)^{-\frac{1}{2}} \quad (24)$$

$$k_t = 8 \left(\frac{2 - \sigma_i}{G_i} + \frac{2 - \sigma_j}{G_j} \right)^{-1} \left(\frac{r_i + r_j}{r_i r_j} \right)^{-\frac{1}{2}} \delta_n^{\frac{1}{2}} \quad (25)$$

where r is the radius of the particles σ the Poisson's ratio; E the Young's modulus, G the shear modulus (given by $G = \frac{E}{2(1+\sigma)}$) and δ_n the magnitude of the deformation in the normal direction. Note as above, when a particle reaches a wall, $r_w \rightarrow \infty$, hence, $\frac{r_s + r_w}{r_s r_w} = \frac{1}{r_s}$.

Description of test cases

The objective of the simulations performed in this work is to investigate the behaviour of a turbulent two-phase flow containing borosilicate glass beads with diameters of 25 μm and 70 μm . Simulations with three different test cases are pursued, which are summarised in table 2.

Geometric data The main test-case involves a particle-laden gas jet issuing into a test chamber, as is described in the experiment ?. The dimensions of the geometry as described in the experimental work are summarised in table 3. Refer to figure 2 for the lay-out of the experiment.

For the simulations, two geometries have been used for the simulation cases, a pipe of length $\frac{x}{D} = 20$ and a pipe of length $\frac{x}{D} = 90$. Both pipes exit in a chamber of width and depth of $\frac{w}{D} = 6.5$ and length of $\frac{l}{D} = 13$. As the chamber in which the jet exits is significantly smaller than the chamber used in the experimental work, full slip

Table 2: Description of test-cases.

Test-Case	Description
1	Two-phase flow with 25 μm particles at solids loading, $m = 1.0$.
2	Two-phase flow with 70 μm particles at solids loading, $m = 1.0$. Note that more than 80% of the range for the 70 μm particles is 62 to 88 μm Hadinoto et al. (2005).
3	Two-phase flow with a binary mixture (both 25 μm and 70 μm particles) at solids loading, $m = 0.5$ for each fraction.

Table 3: Geometric data for the test-case.

Property	Dimension	Units
Pipe Diameter (D)	14.2	mm
Length of pipe (L)	1270.0	mm
$\frac{L}{D}$	90.0	(-)
Length of chamber ($L_{chamber}$)	470.0	mm
Width of chamber ($w_{chamber}$)	470.0	mm
Width of chamber ($w_{chamber}$)	300.0	mm

boundary conditions and a zero pressure gradient have been used as boundary conditions on the chamber walls, to minimize the influence of their presence.

Properties of the particles The physical properties of the borosilicate glass beads as used in the simulations are summarised in table 4.

Properties of the fluid The fluid used in the simulations is air at standard conditions and its properties are summarised in table ??.

¹coefficient of restitution for inelastic particle-particle collisions

²coefficient of restitution for inelastic particle-wall collisions

Table 4: Summary of gas and particle properties used in computations.

Property	Dimension	Units
Diameter of small particles (d_p)	25.0	μm
Diameter of large particles (d_p)	70.0	μm
Density of particles (ρ_p)	2500.0	kgm^{-3}
e_{p-p} ¹	0.94	(-)
e_{p-w} ²	0.15	(-)
Young's modulus (E)	100.0	MPa
Poisson's ratio (σ)	0.25	(-)

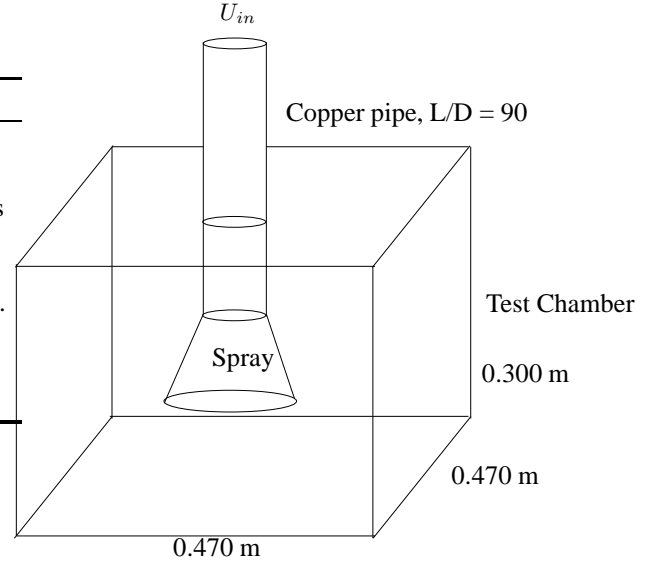


Figure 2: Test chamber dimensions

Table 5: Summary of gas and particle properties used in computations.

Property	Dimension	Units
Temperature (T_{room})	25.0	$^{\circ}\text{C}$
Density of air (ρ_f)	1.204	kgm^{-3}
Reynolds number (Re)	8,400.0	(-)
Viscosity (μ_f)	1.81×10^{-5}	$\text{kgm}^{-1}\text{s}^{-1}$
Kinematic viscosity (ν_f)	1.50×10^{-5}	m^2s^{-1}

Computational mesh

For each simulated geometry, two computational meshes were created. All meshes are suitable for resolving the wall boundary layer, and have 3 mesh points within the $y^+ = 5$ layer. The coarsest geometry for the pipe with length $\frac{L}{D} = 20$ has 55,000 computational cells, and the refined mesh for the same geometry has 260,000 cells. The coarse mesh of the geometry with the pipe length of $\frac{L}{D} = 90$ has 200,000 mesh cells and the fine mesh has around 600,000 mesh cells. Because resolving all the individual particle trajectories takes around 85% of the computational time, the refinement of the mesh does not have a significant impact on the computational time.

Discretisation

The simulations performed in this paper use a finite volume scheme, a second order backward Euler time discretisation and a second order accurate central scheme to approximate the advective terms in the continuity and momentum equations. The solving procedure is made parallel with the MPI libraries. During the simulations,

the CFL number is kept constant at 0.4, leading to a slight variation in time-step over time.

Boundary and Initial Conditions

Experimental data for the single-phase flow are reported at the pipe exit. This reported velocity profile is used to determine the exact mass flow and the centerline velocity to be specified at the inlet of the simulations. Due to mass conservation, the mass flow rate at the pipe exit is constant in the pipe. Using equations (26) & (27), two simultaneous equations are set up to determine the von Karman (κ) and B constants.

$$\dot{m} = \rho_f \int_0^{R-\delta_v} 2\pi r V_1(r) dr + \rho_f \int_{R-\delta_v}^R 2\pi r V_2(r) dr \quad (26)$$

$$U_o = \frac{u_\tau}{\kappa} \ln\left(R \frac{u_\tau}{\nu_f}\right) + B \quad (27)$$

Using the calculated values of κ and B and equations (28) and (30), the inlet velocity profile is produced.

$$V_1(r) = \frac{u_\tau}{\kappa} \ln\left((R-r) \frac{u_\tau}{\nu_f}\right) + B, \quad (28)$$

valid for $0 \leq |r| \leq (R - \delta_v)$, where δ_v is the linear-sublayer,

$$\delta_v = \frac{3\nu_f}{u_\tau} \quad (29)$$

and

$$V_2(r) = \frac{u_\tau^2}{\nu_f} (R - r) \quad (30)$$

valid for $(R - \delta_v) \leq |r| \leq R$. The friction velocity (u_τ) is also required to determine the inlet velocity profile. This is calculated using the following relationship,

$$u_\tau = \sqrt{\frac{\tau_w}{\rho_f}} \quad (31)$$

where the shear wall stress is estimated using the friction factor for a smooth pipe at $Re = 8,400$.

$$\tau_w = \frac{1}{8} f \rho_f \bar{V}^2 \quad (32)$$

and

$$\bar{V} = \frac{\dot{m}}{\pi R^2} \quad (33)$$

Note that the friction factor is estimated using Prandtl's friction law for a fully developed turbulent flow Pope (2000) for a smooth pipe. The values for the above quantities are given in table 6.

The matched velocity profile is set as an inflow condition at the pipe inlet. In addition, in a number of

Table 6: Summary of gas and particle properties used in computations.

Parameter		Units
Friction velocity (u_τ)	0.565	ms^{-1}
Wall shear stress (τ_w)	0.383	Pa
Average velocity (\bar{V})	8.80	ms^{-1}
Linear sublayer (δ_v)	7.87×10^{-5}	m
Mass flow rate (\dot{m})	0.00167	$kg s^{-1}$
von Karman constant (κ)	0.391	(-)
B	3.70	(-)
Friction factor (f)	0.033	(-)

simulations a synthesized turbulent component is added to this flow. The synthesized turbulence is generated by sampling isotropic fluctuations, using the Fourier modes of the fully developed spectrum. The number of Fourier modes which are considered (N) was 600, the turbulent kinetic energy (q_m) is 0.5, the boundary layer thickness (L_t) is $0.0014 m$ and the timescale correlation of the turbulence was estimated at $\tau = 2.48 \times 10^{-4} s$.

In the chamber a laminar flow of constant velocity $0.06 ms^{-1}$ through the top of the box is defined. In the experiment of Hadinoto et al Hadinoto et al. (2005), the top of the box is left open, allowing in order to allow for air entrainment from the surrounding flow. Unfortunately, the exact characteristics of this air flow are not known, making it difficult to predict the correct spreading-rate of the jet as it leaves the pipe.

The walls of the pipe are enforced with a no-slip condition for the velocity and pressure is extrapolated onto the walls from the fluid. The pressure boundary conditions were interpolated from downstream at the inlet of the pipe and the inlet of the chamber walls. It is found that interpolation from downstream improves the results over the more common zero-gradient boundary conditions for pressure.

As the chamber in which the jet exits in the simulations is significantly smaller than the chamber used in the experimental work, full slip boundary conditions and a zero pressure gradient have been used as boundary conditions on the chamber walls, to minimize the influence of their presence.

Particle Injection The particles are injected at the pipe inlet (noted as $L/D = 0$) with a solids loading very near of $m = 1.0$. The injection timing is set so as to compensate for the difference in the solids loading at each injection. This will produce an overall solids loading very near to 1.0 spread out through the geometry. Assuming a uniform placement of particles at the inlet,

the location of each particle at the pipe inlet is known. A random component is added to the spatial coordinates of the particle. Also, the particles are given a random component on all velocity directions. Some form of initial dispersion, caused by velocity fluctuations in the radial and azimuthal direction, is crucial to obtain an accurate representation of the flow behaviour of the particles.

70 μm particles A particle size distribution (PSD) is used for the 70 μm particles (the particle diameter range was between 62 μm to 88 μm). The number based distribution used was uniform (i.e. the number based probability to find a particle is the same). Since the PSD must be volume based, the cumulative density function (cdf) of the number based distribution is raised to 1/3 in order to obtain the volume based cdf. Note that the solids loading for the 70 μm particles is 1.0.

25 μm and 70 μm particles The procedure described for the 70 μm particles is repeated for the binary mixture. A PSD is used with a cdf of 95% 25 μm and 5% 70 μm . This is because a solids loading of 0.5 is required for each fraction. Therefore the ratio of the number of particles for each fraction is given by,

$$\frac{n_{70}}{n_{25}} = \left(\frac{d_{p25}}{d_{p70}} \right)^3 = 0.05.$$

Results and Discussion

Up to now, simulations for test-cases 2 and 3 have been run, although not all test-cases have sufficient statistics to draw firm conclusions. The simulations are run on 8 cores in parallel.

Comparison of mesh refinement

Two different meshes were used to simulate the small pipe geometry; the coarse mesh having approximately 55,000 mesh cells and the fine mesh having approximately 260,000 mesh cells, meaning a refinement of about 1.75 in all directions. Figure 3 shows the effect of mesh refinement on the predicted centerline velocity at the pipe exit. It can be seen that the mesh refinement has very little effect. A similar conclusion can be drawn for the results presented in Figure 4, showing the magnitude of the fluctuations at the pipe exit, and Figure 5 showing the centerline velocity downstream from the pipe exit. It can be seen that especially the fine mesh needs to be run for longer, as the statistics are not yet steady.

Comparison of SGS LES models

Three different LES models for closing the SGS stresses are employed. The results are shown in Figures 6,7, 8 &

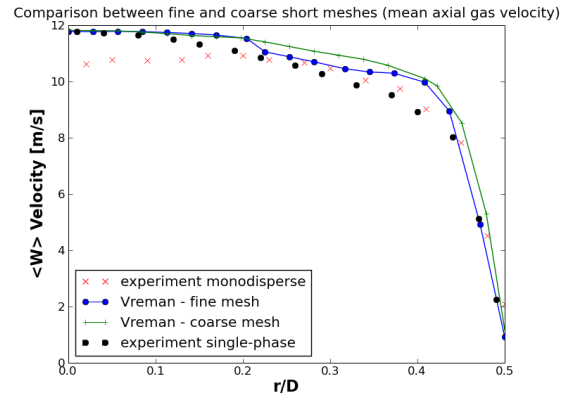


Figure 3: The simulation results of the mean axial velocity at the pipe exit ($\frac{x}{D} = 0$) from the fine and coarse mesh, compared with the single phase and multiphase data.

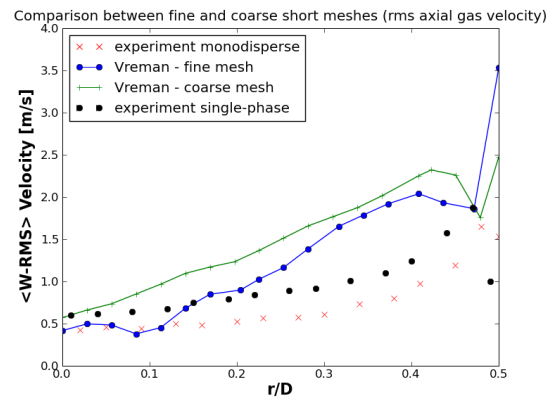


Figure 4: The simulation results of the root mean square of the velocity fluctuations at the pipe exit ($\frac{x}{D} = 0$) from the fine and coarse mesh, compared with the single phase and multiphase data.

9. In Figure 16 all models seem to overpredict the mass flow rate at the pipe exit. However, a good correlation between the experimental results is achieved especially the Vreman model. This is better illustrated in Figure 8 where the Vreman model is in good agreement with the experimental results (particularly near the pipe exit). The axial and radial rms velocities, however, are not predicted well by the models. This is because there are not enough statistical data and also this comparison is for the short pipe.

Effect of pipe length

Fluid Statistics There is a strong effect of the length of the pipe on the fluid velocity statistics. Figure 10

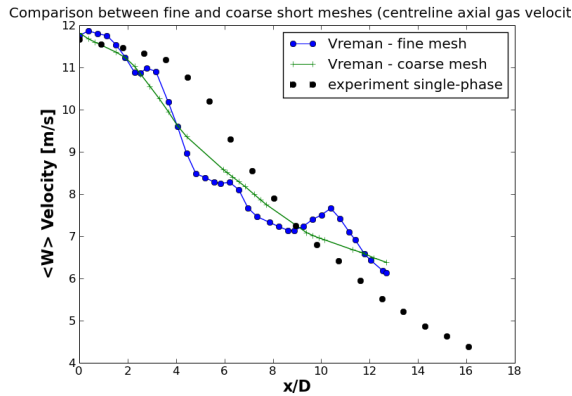


Figure 5: The simulation results of the average centerline velocity after the pipe exit (from $\frac{x}{D} = 0$) from the fine and coarse mesh, compared with the single phase and multiphase data.

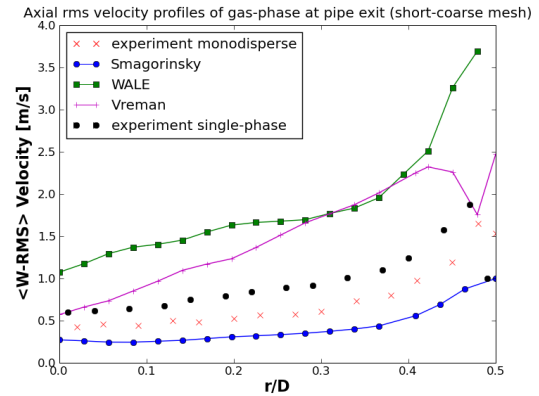


Figure 7: The simulation results of the root mean square of the velocity velocity fluctuations at the pipe exit exit ($\frac{x}{D} = 0$) as a result from the different SGS closure models compared to experimental data.

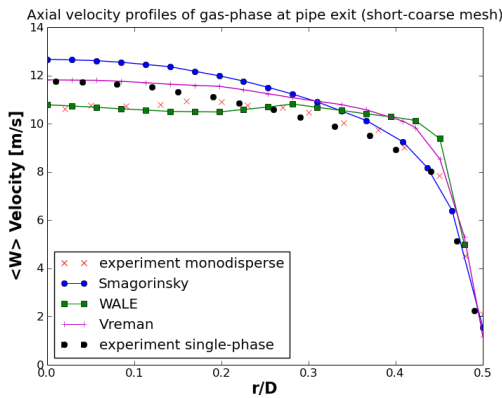


Figure 6: The simulation results of the average centerline velocity at the pipe exit ($\frac{x}{D} = 0$) as a result from the different SGS closure models compared to experimental data.

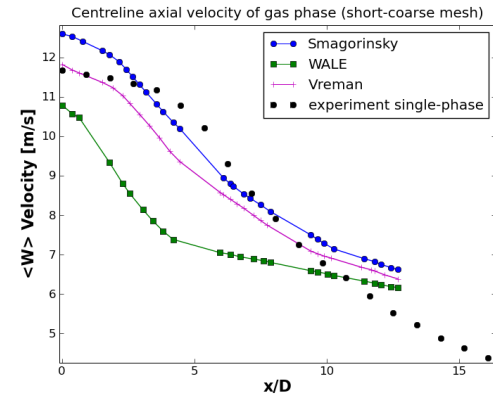


Figure 8: The simulation results of the average centerline velocity after the pipe exit (from $\frac{x}{D} = 0$) as a result from the different SGS closure models compared to experimental data.

shows the mean axial flow velocity directly at the pipe exit for the short pipe ($\frac{l}{D} = 20$) and the long pipe ($\frac{l}{D} = 90$) compared to experimental data. The data of the long pipe is a very good match to the experimental data. For both cases, it seems that the mass flow is slightly overestimated at the inlet of the pipe. Figure 11 shows the root mean square of the velocity fluctuations in the axial direction resulting from the simulation with the short pipe compared, the simulation with the long pipe and the comparison with experimental data. Both predictions are reasonable and there is no clear difference. Figure 12 shows the root mean square of the velocity fluctuations in the radial direction resulting from the simulation with the short pipe compared, the simulation with the long pipe and the comparison with experimen-

tal data. Both predictions underestimate the magnitude of the fluctuations.

Particle Statistics There is also a strong effect of the pipe length on the particle velocity statistics; the results possibly show that the longest pipe, with length $\frac{l}{D} = 90$ is not long enough to achieve fully developed flow for the particles. Figure 13 shows the mean particle velocity in the axial direction for the long pipe, the short pipe, and the experimental data. There is a strong improvement for the longer pipe, but the match is not completely satisfactory.

Figures 14 and 15 show the root mean square of the particle velocity in the axial and radial directions, respectively. Although the trends in both figures seem to be

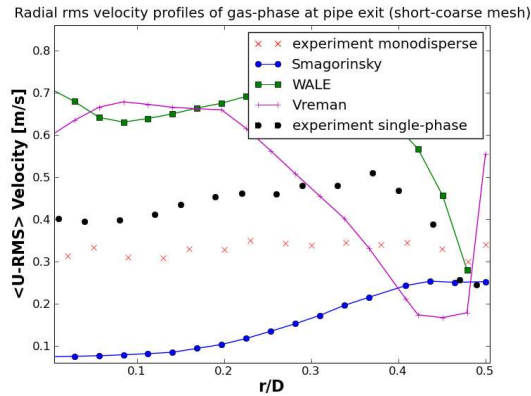


Figure 9: The simulation results of the average axial velocity component at the pipe exit ($\frac{x}{D} = 0$) as a result from the different SGS closure models compared to experimental data.

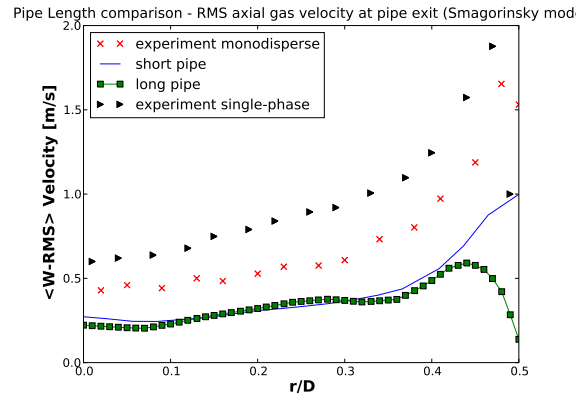


Figure 11: The simulation results of the root mean square of the fluid fluctuating axial velocity component at the pipe exit ($\frac{x}{D} = 0$) from the short pipe ($\frac{l}{D} = 20$) and the long pipe ($\frac{l}{D} = 90$) compared to experimental data.

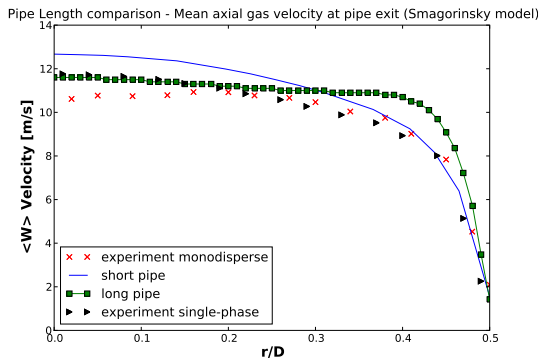


Figure 10: The simulation results of the average fluid axial velocity component at the pipe exit ($\frac{x}{D} = 0$) from the short pipe ($\frac{l}{D} = 20$) and the long pipe ($\frac{l}{D} = 90$) compared to experimental data.

correctly predicted, there seems to be an offset in the predictions compared to the experimental data.

Bimodal particle mixture

A case employing the Smagorinsky SGS model including van Driest Dampening was performed including a binary particle mixture, with particles of $d_p = 25\mu m$ and $d_p = 70\mu m$ with a 50:50 relative volumetric proportion with a total mass loading of 1.0.

Fluid velocity statistics Figures 16 and 17 show the mean fluid velocity in the axial direction and the root mean square of the fluid velocity fluctuations in the axial direction, respectively. Both are compared to the experimental findings. The results show a fairly good

prediction.

The prediction of the root mean square of the velocity fluctuations, compared to the experiments, as shown in figure 18 is not as good, probably due to a lack of statistical values.

Particle statistics As the experiments have been performed with phase doppler anemometry (PDA), the velocity statistics of the small and the large particles in the binary mixture have been determined separately. Although very similar, some changes have been found in the statistics of the small particles compared to the large ones experimentally. Figures 19, 20, and 21 show the simulation predictions of the two individual particle species, comparing them to the experimental results. Although the predictions are fair, there seems to be no significant difference between the two particles in the simulations. This is probably due to a lack of statistics for the particulate phase.

Conclusions

This paper presents Large Eddy Simulation (LES) modelling work and comparing this work to the experimental data as presented by prof. J. Curtis and co-workers. The simulations have been run without any empirical parameters and material properties have been chosen to accurately reflect the properties of the fluid and the particles.

Generally, the simulations are too short to draw strong conclusions. However, a few conclusions can

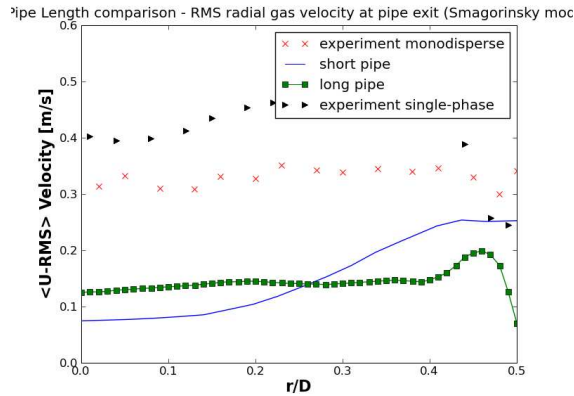


Figure 12: The simulation results of the root mean square of the fluid fluctuating radial velocity component at the pipe exit ($\frac{x}{D} = 0$) from the short pipe ($\frac{l}{D} = 20$) and the long pipe ($\frac{l}{D} = 90$) compared to experimental data.

be drawn from the results presented so far. The first conclusion is that the simulation results seem to be fairly independent of mesh resolution. Changing the mesh from 55,000 cells to 260,000 cells hardly affects the results. Moreover, the results from the WALE and Vreman LES models accurately capture the presence of the wall, without the necessity of applying van Driest dampening. The application of such wall dampening is computationally expensive in parallel simulation runs.

An important aspect of the simulations, is the size of the geometry. The simulation with the shortest geometry, with a pipe of $\frac{l}{D} = 20$, is too short for the fluid and particles to be fully developed. There are also concerns that the chamber in which the pipe exits is too small to reflect an accurate spreading of the jet. The uncertainty of the flow in the chamber in the experimental work makes it difficult to match with the simulations.

Future work

The most important goal for the future is to perform longer simulations, so better statistics can be obtained for the largest geometry. Once this is achieved, the effect of varying the following properties in the simulation will be performed:

- The size of the chamber. The size of the chamber will affect the spreading rate of the jet. If this will also affect the dispersion of particles will be researched.
- The van Driest dampening parameters at the wall.

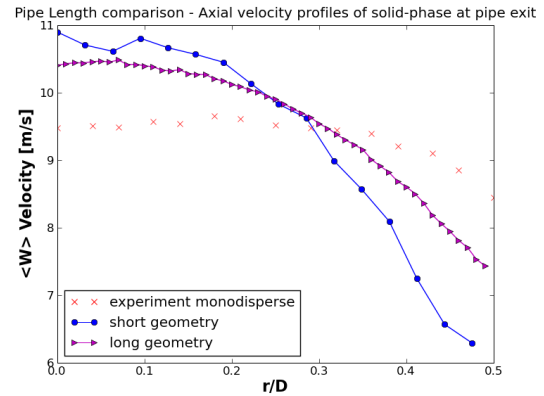


Figure 13: The simulation results of the average axial particle velocity component at the pipe exit ($\frac{x}{D} = 0$) from the short pipe ($\frac{l}{D} = 20$) and the long pipe ($\frac{l}{D} = 90$) compared to experimental data.

This may have an important effect on the center line velocity.

- The magnitude of the SGS constants. All the SGS models contain a constant, and although in theory the magnitude of the constant should not effect the flow characteristics this is likely not to be true for this case, which has a fairly low Re number.
- The properties of the particles. The fluid and particle velocities are highly affected by the collisions of the particles, which are affected by the material properties.

References

P.A. Cundall and O.D.L. Strack. A discrete numerical model for granular assemblies. *Geotechnique*, 29:47–65, 1979.

J. Grifoll and F. Giralt. The near wall mixing length formulation revisited. Technical report, 2000.

K. Hadinoto, E.N Jones, C. Yurteri, and J. S. Curtis. Reynolds number dependence of gas-phase turbulence in gas-particle flows. *Int J. Multiphase Flow*, 31:416–434, 2005.

S.B. Kuang, K.W. Chu, A.B. Yu, Z.S. Zou, and Y.Q. Feng. Computational investigation of horizontal slug flow in pneumatic conveying. *Ind. Eng. Chem. Res.*, 47: 470–480, 2008.

F. Nicoud and F. Durcos. Subgrid-scale stress modelling based on the square of the velocity gradient tensor. *Flow, Turbulence and Combustion*, 62:183–200, 1999.

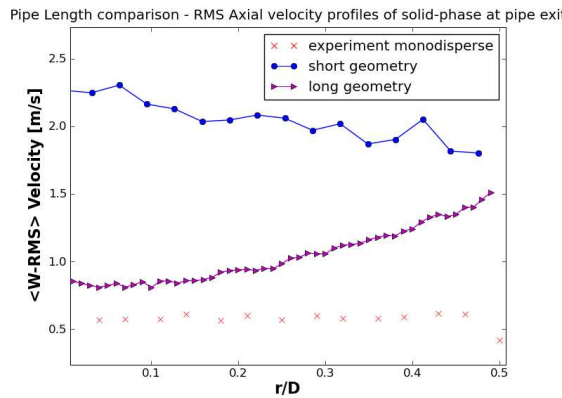


Figure 14: The simulation results of the root mean square of the particle fluctuating axial velocity component at the pipe exit ($\frac{x}{D} = 0$) from the short pipe ($\frac{l}{D} = 20$ and the long pipe ($\frac{l}{D} = 90$) compared to experimental data.

S. B. Pope. *Turbulent Flows*. Cambridge Univ. Press., 2000.

Y. Tsuji. Discrete particle simulation of gas-solid flows. *KONA Powder and Particle*, 11:57–68, 1994.

Y. Tsuji, T. Tanaka, and T. Ishida. Lagrangian numerical simulation of plug flow of cohesionless particles in a horizontal pipe. *Powder Technology*, 71:239–250, 1991.

H. Versteeg and W Malalasekera. *An Introduction to Computational Fluid Dynamics, the Finite Volume Method*. Prentice Hall, 2007.

A.W. Vreman. An eddy-viscosity subgrid-scale model for turbulent shear flow: Algebraic theory and applications. *Phys. Fluids*, 16:3670–3681, 2004.

M. Weickert, G. Teike, O. Schmidt, and M. Sommerfeld. Investigation of the les wale turbulence model within the lattice boltzmann framework. *Computers and Mathematics with Applications*, in press, 2009.

C. Y. Wen and Y. H. Yu. Mechanics of fluidization. *Chemical Engineering Progress Symposium Series*, 62: 100–111, 1966.

D. C. Wilcox. *Turbulence Modeling for CFD*. DCW Industries, 1998.

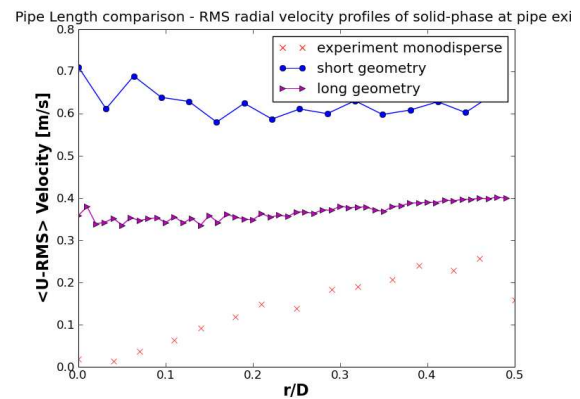


Figure 15: The simulation results of the root mean square of the particle fluctuating radial velocity component at the pipe exit ($\frac{x}{D} = 0$) from the short pipe ($\frac{l}{D} = 20$ and the long pipe ($\frac{l}{D} = 90$) compared to experimental data.

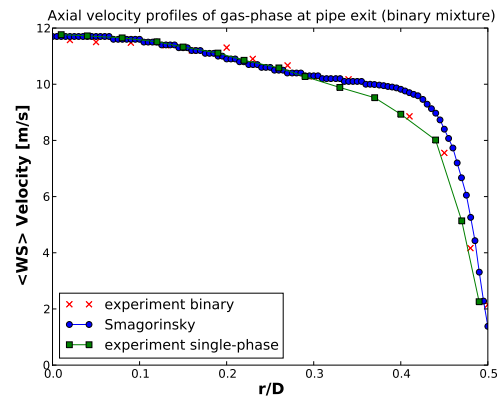


Figure 16: The simulation results of the average fluid axial velocity component at the pipe exit ($\frac{x}{D} = 0$) including the binary particle mixture compared to experimental results.

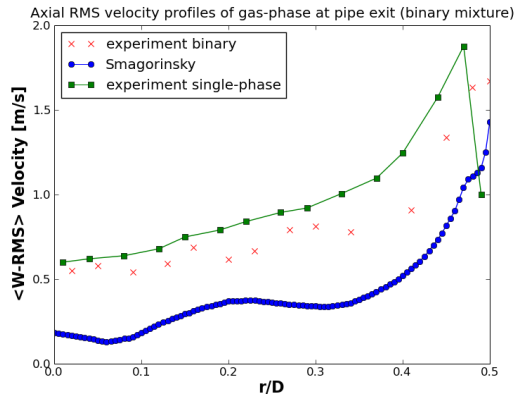


Figure 17: The simulation results of the root mean square of the fluid fluctuating axial velocity component at the pipe exit ($\frac{x}{D} = 0$) for the dispersed flow containing the binary particle mixture.

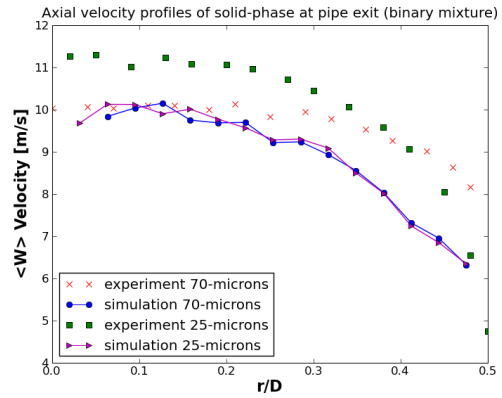


Figure 19: The simulation results of the average axial particle velocity component at the pipe exit ($\frac{x}{D} = 0$) of the two particle species.

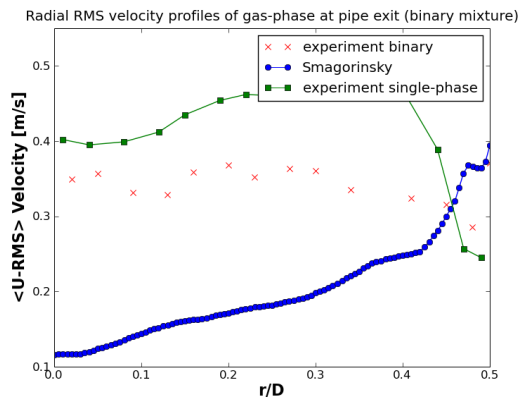


Figure 18: The simulation results of the root mean square of the fluid fluctuating radial velocity component at the pipe exit ($\frac{x}{D} = 0$) of the flow containing the binary mixture of particles compared to experimental data.

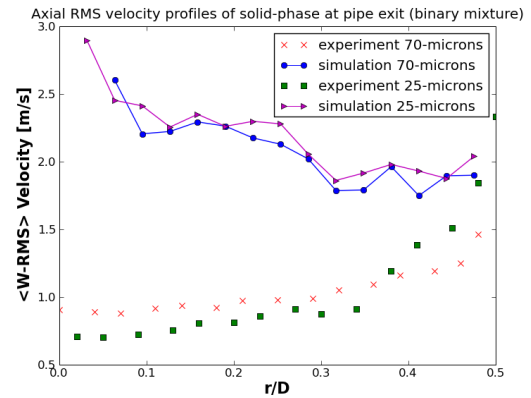


Figure 20: The simulation results of the root mean square of the particle fluctuating axial velocity component at the pipe exit ($\frac{x}{D} = 0$) for the two particle species in the binary mixture.

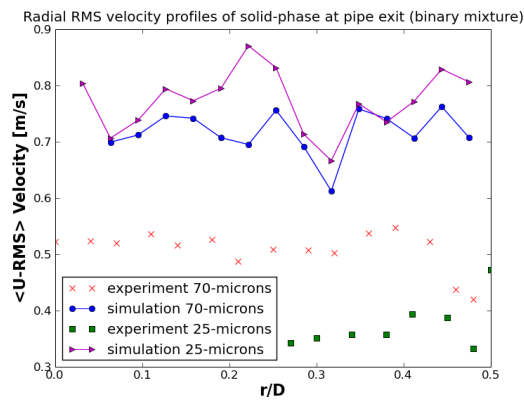


Figure 21: The simulation results of the root mean square of the particle fluctuating radial velocity component at the pipe exit ($\frac{x}{D} = 0$) for the two particle species in the binary mixture.